Journal of Power Sources 576 (2023) 233197

Contents lists available at ScienceDirect

Journal of Power Sources

journal homepage: www.elsevier.com/locate/jpowsour

Realizing high energy density supercapacitors assisted by light-induced charging

Janardhanan R. Rani [b,c], Nayan Chandra Das [c], Minjae Kim [c], Ranjith Thangavel [d,e], Sung Tae Kim [c], Yun Sung Lee [d], Jae-Hyung Jang [a,c,f,*]

[a] KENTECH Institute for Energy Materials and Devices, Korea Institute of Energy Technology, Naju, 58330, South Korea
[b] Department of Physics, University College, Thiruvananthapuram, 695034, Kerala, India
[c] School of Electrical Engineering and Computer Science, Gwangju Institute of Science and Technology, Gwangju, 61005, South Korea
[d] Faculty of Applied Chemical Engineering, Chonnam National University, Gwangju, 61186, South Korea
[e] School of Energy Science and Engineering, Indian Institute of Technology, Guwahati, 781039, India
[f] Department of Energy Engineering, Power Semiconductor Concentration, Korea Institute of Energy Technology, Naju, 58330, South Korea

HIGHLIGHTS

- Harvested visible light for charging supercapacitors.
- Charging was achieved through illuminating the supercapacitor using blue laser diode.
- The supercapacitor exhibited a light induced-charging voltage of 354 mV, without any external bias.
- The illuminated cell exhibited an areal energy density of 2.5 times higher than non-illumiated cell.

GRAPHICAL ABSTRACT

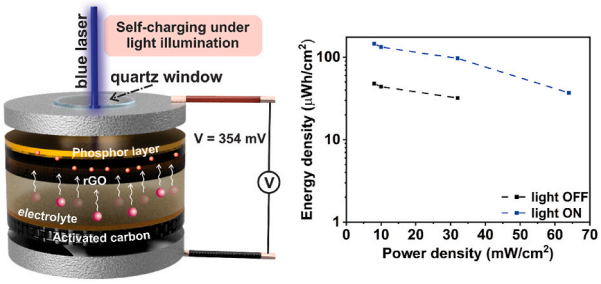

ARTICLE INFO

Keywords:
Carbon based supercapacitors
Reduced graphene oxide
Light-induced charging
Renewable energy

ABSTRACT

The increasing demand for energy storage devices has initiated research on alternative sustainable energy storage mechanisms, such as supercapacitors. Here, we report a skillful design strategy that harvests visible light energy and has immense potential applications in boosting the storage capacity of supercapacitors – one of the energy storage devices. A down-conversion phosphor layer is introduced over a reduced graphene oxide-based supercapacitor electrode having an optical window to harvest visible light. The fabricated cell exhibits an excellent areal energy density of 233 μWh/cm^2 (at an areal current density of 4 mA/cm^2 for the voltage ranging from 2 to 4.25 V) under optical illumination, which is 2.5 times higher than that achieved without illumination. Under light illumination, the cell operates across a high voltage range (0–4 V) and current density (40 mA/cm^2) and shows a light-induced charging voltage of 354 mV, without any external bias. Thus, such exceptional supercapacitor performance generates significant possibilities for developing novel energy storage devices with high energy and power densities, through which portable devices can be charged using visible light.

* Corresponding author. KENTECH Institute for Energy Materials and Devices, Korea Institute of Energy Technology, Naju, 58330, South Korea.
E-mail address: jjang@kentech.ac.kr (J.-H. Jang).

https://doi.org/10.1016/j.jpowsour.2023.233197
Received 28 July 2022; Received in revised form 18 April 2023; Accepted 11 May 2023
Available online 22 May 2023

1. Introduction

Renewable energy technologies play an essential role in reducing greenhouse gas emissions, and the importance of developing renewable energy conversion techniques has gained widespread recognition [1]. Owing to the highly intermittent characteristics of renewable energies, such as solar and wind power generation, power grids incorporating a large percentage of renewables require high energy storage capacity for their stable operation. Supercapacitors, which are an emerging electrochemical energy storage technology, have attracted significant attention owing to their excellent characteristics, such as high power density, operational safety, ultra-fast charging/discharging capability, and long cycle life [2,3]. Although supercapacitors exhibit quick charging/discharging capability and a longer lifetime, their energy densities are lower than those of Li/Na/K-ion batteries, which hinders their use in applications requiring high energy density [4–6]. Currently, batteries are used in high-energy-density applications. By developing a technology to increase the energy density of supercapacitors comparable to that of batteries, supercapacitors will become useful for both high energy and high power density applications. Numerous strategies to enhance the energy density of supercapacitors include (i) doping the active electrode using pseudocapacitive materials [7], transition metal/rare earth metal oxides [8], and conducting polymers [9]; (ii) fabricating honeycomb-like 3-dimensional (3-D) graphene structures [9] and carbon nanotube (CNT) sponges [10], and integrating metal tungstate with graphene electrodes [11]; (iii) incorporating metal ferrites [12] and manganites [13]; (iv) using large surface area-activated carbon electrode [14]; (v) modifying surface functional groups [15], including heteroatoms (N, O) [16], and doping with electronically conducting polymers such as polyaniline [17] and polypyrrole [18]. However, the aforementioned strategies have not demonstrated adequately high energy densities; therefore, novel strategies should be developed to enhance the energy density of supercapacitors. Additionally, self-charging devices were proposed for sustainable energy storage devices [19]. For this, triboelectric/piezoelectric materials were integrated with the electrochemical cell to convert mechanical energy into electrical energy [20]. Such devices provide uninterrupted power supply owing to its self-charging capability. However, piezoelectric materials require longer time to charge the device. Novel strategies should be explored for the development of self-sustaining energy storage devices.

In this study, a skillful strategy was introduced to increase the energy density of supercapacitors by harnessing optical energy. A supercapacitor electrode was fabricated using a down-conversion phosphor, Ce doped yttrium aluminium garnet (YAG:Ce^{3+}), a material that emits visible light upon optical excitation using ultraviolet or visible light), along with reduced graphene oxide (rGO) scrolls [21]. The YAG:Ce^{3+} phosphor exhibits broad absorption spectra (250–470 nm) with a peak absorption wavelength of 450 nm [22]. The phosphor material was chosen for the following two reasons: (i) phosphors exhibit high photoconductivity and therefore, effectively release additional electrons under optical illumination, and (ii) these additional electrons significantly improve the rate of Faradaic intercalation redox reaction, resulting in exceptionally high energy density values. During photo-excitation, Ce^{3+} ions oxidise to Ce^{4+}, releasing electrons that are transported to the active electrode, enhancing the electrical conductivity, which causes the Faradaic intercalation redox reaction between the electrode and electrolyte ions.

2. Methods

2.1. Preparation of GO

GO was prepared using Hummer's method. Graphite powder (8 g, sigma-Aldrich; purity 99.997%) was first pre-oxidized using H_2SO_4 (120 mL, sigma-Aldrich, 99.9%), $K_2S_2O_8$ (4 g, Sigma-Aldrich, 99.9%), and P_2O_5 (4 g, sigma-Aldrich, 99.9%) at 80 °C. The solution was washed until the pH became neutral. The oxidized graphite powder (4 g) was placed in cold (0 °C) concentrated H_2SO_4 (80 mL), and $KMnO_4$ (12 g) was added subsequently while stirring in an ice-bath. The mixture was then stirred at 35 °C for 2 h, after which deionized water (560 mL) and 30% H_2O_2 solution (40 mL) were added to the mixture to stop the reaction. For removing the metal ions, this mixture was washed by repeated centrifugation and filtration with 5% HCl solution. For getting the GO powder, the resultant mixture was dried under vacuum at 50 °C for 6 h. The details of the preparation methods have been explained in a previously published study [23].

2.2. Preparation of MnO_2 encapsulated within rGO scrolls (GMS)

To synthesise the MnO_2-rGO scrolls, graphene oxide (GO) (0.6 g, sigma-Aldrich; purity 99.997%) was dispersed in 50 mL water, and 0.15 g MnO_2 (sigma-Aldrich, 99.97%) was added to the dispersion and sonicated for 1 h 30 min using an ultrasonic reactor. The mixture was then centrifuged at 10,000 rpm for 15 min, followed by filtration. The sonication, centrifugation, and filtering were repeated multiple times, and the solution was dried overnight at 110 °C to form a powder. The powder was further annealed at 400 °C under a nitrogen atmosphere for 2 h to remove impurities. The MnO_2 particles attached to the GO powder, which resulted in the bending of the GO sheets. Finally, the GO sheets formed scrolls and wrapped around the MnO_2 particles. SEM images of the powder confirmed that the synthesised powder consisted of MnO_2 particles encapsulated within the rGO scrolls. The nitrogen-annealed MnO_2 encapsulated by rGO scrolls was termed as GMS and was used to fabricate the supercapacitors.

2.3. Preparation of rGO wrapped phosphor material (rGOP)

The phosphor YAG:Ce^{3+} was mixed with the rGO solution at a concentration of 0.7 mg/mL, followed by continuous sonication for 4 h. The mixture was centrifuged at 10,000 rpm for 15 min. Sonication, centrifugation, and filtering were conducted multiple times, followed by overnight drying at 110 °C to obtain the mixed rGO-phosphor composite powder samples. The powder was annealed at 1200 °C under a reducing atmosphere (N_2/H_2). The final powder consisted of rGO-wrapped phosphor particles, which were labeled as rGO-Phosphor (rGOP). GMS and rGOP were mixed in a ratio of 4:1 to form GMS-rGOP composites that were labeled as GMSP.

2.4. Cell fabrication

A composite anode slurry was synthesised using a 15:3:2 mixture of active materials (GMSP), Ketzen black (KB), and teflonised acetylene black (TAB) in ethanol, followed by pressing on a 200 mm^2 nickel steel mesh current collector. The pressed slurry was dried at 160 °C for 4 h in a vacuum oven. An active material with a mass of 8 mg/cm^2 was used for the cell fabrication. The electrodes were separated by a porous polypropylene film (Celgard 3401, USA), and an ionic electrolyte, 1 Ethyl 3 methylimidazolium tetrafluoroborate $EMIMBF_4$, was used. Finally, a layer of rGOP powder (1 mg) coating was deposited on the electrode material of the GMSP. The electrochemical performances of the hybrid supercapacitor cells were investigated for different voltage windows (0–1 V, 2–4.25 V, and 0–4 V) using a battery tester (WBCS 3000, WonATech, Korea).

2.5. Fabrication of the light-harvesting supercapacitor

Complete stainless steel electrodes are not suitable for fabricating cells operating under optical illumination; a specially designed stainless steel electrode with a 9 mm diameter quartz window was used to fabricate the light-harvesting supercapacitor cells. The quartz window allowed visible light to fall on the electrode material. Both sides of the quartz window were coated with a transparent conductor - indium tin

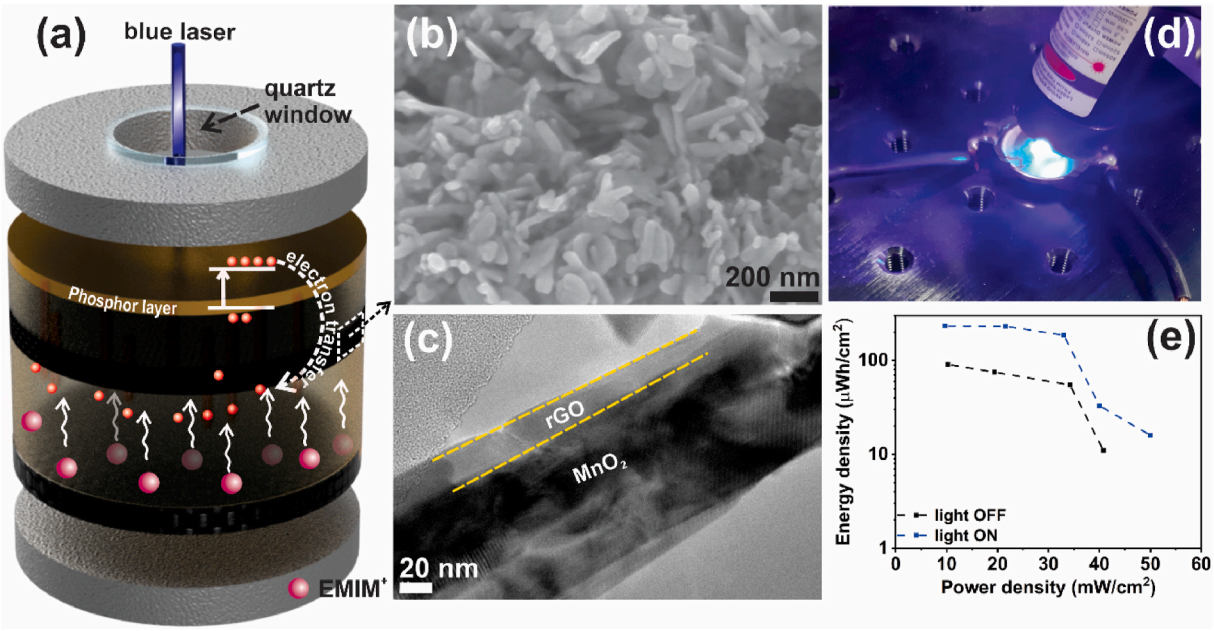

Fig. 1. (a) The schematic structure of the supercapacitor with the electron transfer from the phosphor layer to the electrode (the light and dark pink spheres denote EMIM and the orange spheres denote electrons), (b) SEM image showing the scroll structure of the MnO_2 encapsulated by rGO scrolls, (c) HRTEM image showing the enlarged view of the single scroll in Fig. 1(b), (d) Digital photograph of the supercapacitor in the operating mode under blue laser diode illumination, (e) Ragone plot of the supercapacitor in the 2–4.25 V voltage range, exhibiting an energy density of 233 μWh/cm^2. (For interpretation of the references to colour in this figure legend, the reader is referred to the Web version of this article.)

oxide (ITO) before cell fabrication. The power density of the laser is 210 mW/cm^2. The tested cell has 20-mm-diameter and 3-mm-thickness.

2.6. Characterizations

Scanning electron microscopy (SEM) (JEOL, JSM-6700 F) and high resolution transmission electron microscopy/selected area electron diffraction (HRTEM/SAED) (JEM.ARM.200 F) were used to analyse the morphological, structural, and compositional properties of the GMS, rGOP, and GMSP powders. The current-voltage characteristics of the fabricated rGO and GMSP scrolls were measured using a Keithley 4200 semiconductor parameter analyser at room temperature.

2.6.1. Current-voltage measurements

For the current-voltage measurements, rGO and GMSP were deposited on the ITO-coated glass substrate. The substrate was cleaned using acetone, isopropanol, and deionized (DI) water in an ultrasonic bath for 5 min each, 3 g of GMSP powder was dispersed in 9 mL water, and the solution was sonicated for 30 min. Then, the solution was drop-cast onto the substrate and subsequently annealed at 90 °C for 10 min using a hotplate. Finally, a 100-nm-thick Pt top electrode was deposited using electron beam evaporation. The fabricated two-terminal devices were subjected to current-voltage characterization. To study the light illumination response of the devices, the current-voltage characteristics of the device were measured under optical illumination with a blue laser diode and under dark conditions.

2.6.2. Ultraviolet photoelectron spectroscopy (UPS) measurements

Silicon was used as the substrate for UPS measurements. The substrate cleaning and deposition methods were similar to those mentioned in the current–voltage (*I–V*) measurement section. An rGO-phosphor solution was also prepared and drop-cast on the Si substrate and subsequently annealed at 90 °C for 10 min for comparison.

2.6.3. Cyclic voltammetry (CV) measurements for lowest unoccupied molecular orbital (LUMO) calculations

For CV measurements, ITO-coated glass was used as the substrate, and the GMSP and rGO films were deposited, as described in the Photoconductivity Measurement Section. A standard three-electrode cell with a Ag/AgCl reference electrode and a Pt wire counter electrode was used to measure the CV characteristics (CV curves) of the films. An aqueous solution of (0.5 M H_2SO_4 was used as the electrolyte. The films deposited on ITO were utilised as working electrodes in a three-electrode configuration using a computerized potentiostat/galvanostat.

3. Results and discussion

In this study, the charge storage efficiency was successfully enhanced by illuminating the supercapacitor using a blue laser diode (450 nm), which matched well with the peak absorption wavelength of the YAG: Ce^{3+} phosphor. Thus, photo-excitation facilitated the enhancement of storage capacity, and thereby, a high energy density was achieved in the supercapacitor. Without light illumination, the areal energy density was 91 μWh/cm^2 at an areal current density of 4 mA/cm^2. When the supercapacitor was illuminated with a blue laser diode, an energy density of 231 μWh/cm^2 was achieved at an areal current density of 4 mA/cm^2 for the voltage range of 2–4.25 V, which enhanced the energy density by 2.5 times compared with that achieved without light illumination. This is one of the highest energy density values reported thus far. Furthermore, an exceptional light-induced charging capability was demonstrated with phosphor-incorporated supercapacitors. A light-induced charging voltage of up to 354 mV was achieved by illuminating the cell using a blue laser. Several recent studies have focused on harvesting light through solar cell-supercapacitor and/piezoelectric-supercapacitor hybrid devices [24–27]. However, notably, the proposed design is simpler and entirely different from those of previous studies, and light-induced charging was efficiently achieved by including a phosphor material.

A specially designed stainless-steel electrode with a quartz window

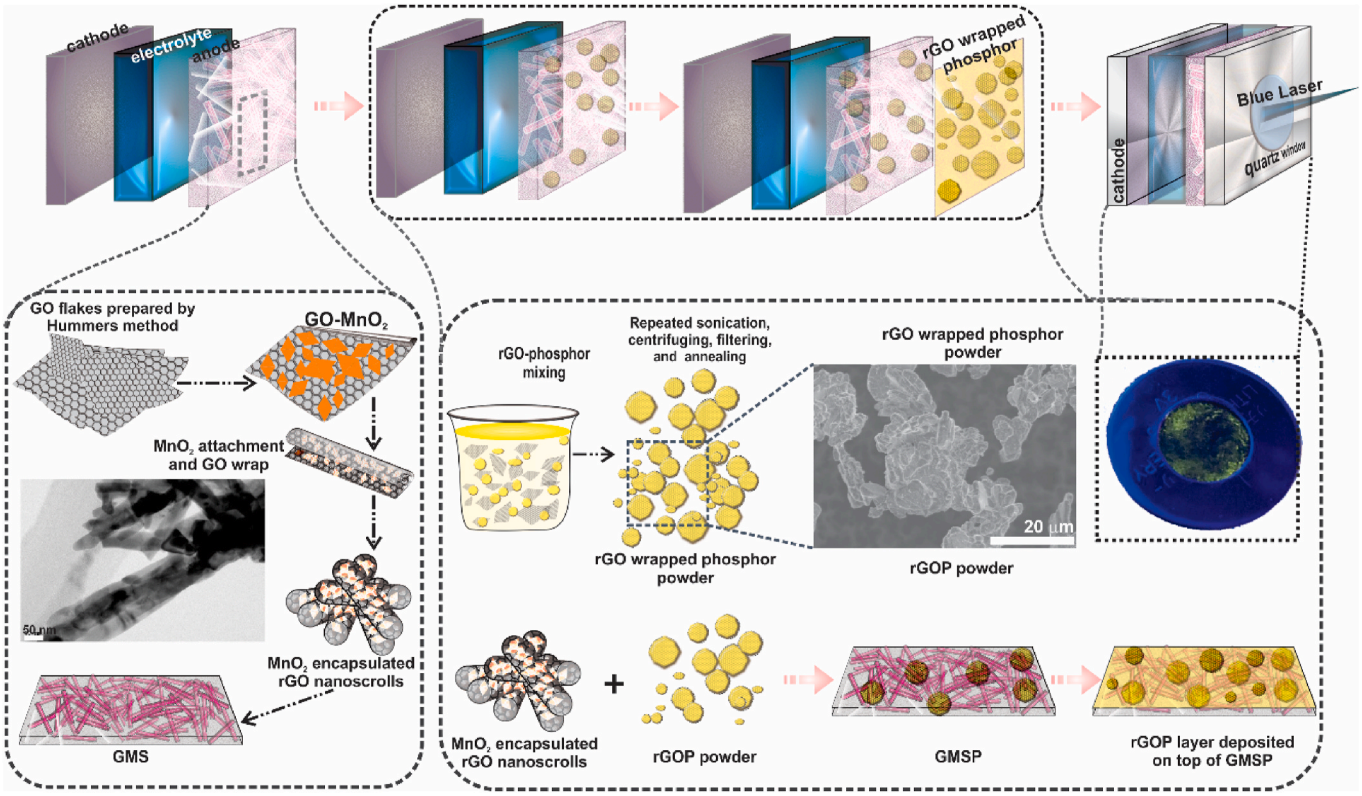

Fig. 2. Schematic diagram illustrating the synthesising procedure of the GMS, GMSP powder materials, and the supercapacitor cell.

was used to fabricate cells operating under optical illumination. The quartz window facilitated the incidence of visible light on the electrode material. A blue laser diode was used to illuminate the cell through this quartz window, as shown in Fig. 1(a). The layers of the electrode are shown separately in the schematic diagram. To incorporate phosphor particles into the electrode, first, the phosphor particles were wrapped using reduced graphene oxide (rGO) and is described as (rGOP), which was deposited as the top layer on the active electrode, absorbing visible light, and generating free electrons. The active electrode was fabricated by mixing rGOP with MnO_2-encapsulated rGO scrolls (GMS) and was labeled as GMSP. In previous studies, it was observed that MnO_2 added to rGO facilitates scroll formation and achieves better supercapacitive performance [28]. We have also fabricated three separate supercapacitors using pure MnO_2, MnO_2-rGO composite and rGO electrodes. We investigated the electrochemical performance with and without light. Fig. S1 depicts the galvanoscopic charge-discharge curves of those supercapacitors, which shows inferior performance even under light illumination. Thus, we choose GMSP as electrode material.

Under optical illumination, the top phosphor material in the cell absorbed light and then re-emitted photons with a longer emission wavelength of 550 nm. The electrons released through the photo-oxidation of Ce^{3+} ions in the phosphor material were then transported to the GMSP active material electrode and enhanced the Faradaic intercalation redox reaction with electrolyte ions.

Fig. 1(b) shows scanning electron microscopy (SEM) images of the GMS material depicting the formation of the scroll structure in the active material.

Fig. 1(c) shows the HRTEM images of the single scroll in Fig. 1(b). Fig. 1(d) shows a digital photograph of the supercapacitor in the operating mode. Fig. 1(e) shows the Ragone plot of the supercapacitor, which exhibited a high energy density of 233 μWh/cm^2. Under both conditions (dark and illumination), the energy density decreases as output power increases.

A video of the supercapacitor working under light illumination is provided in the Supplementary Information.

The morphology and distribution of MnO_2 particles on rGO sheets were observed using a scanning electron microscope (SEM) and are shown in Figs. S2(a–d). The scroll structure of the rGO sheets was visible in the SEM images. Furthermore, HRTEM was used to observe the scroll structure of the GMS samples, as shown in Figs. S2(e–g). Morphological analyses using SEM and HRTEM showed the formation of scroll structures in which flat rGO sheets were transformed to scrolls through the attachment of MnO_2 particles. Size distribution analysis of the images revealed that the formed scrolls were approximately 300–350 nm in length. An expanded view of a single scroll structure is shown in Figs. S2 (f) and (g), and the selected area electron diffraction (SAED) pattern is shown in Fig. S2(h). In summary, the rolling of the rGO layers in one or more directions resulted in the formation of GMS [29].

A schematic diagram of the manufacturing procedure and the supercapacitor cell design for harvesting light are shown in Fig. 2.

The electrochemical properties of the fabricated supercapacitor with and without light illumination in a voltage range of 0–4 V are shown in Fig. S3. Fig. S3 (a) shows the CV curves measured with and without light illumination at a scan rate of 20 mV/s. Figs. S3(b) and (c) show the GCD curves measured with and without light illumination at various current densities. The areal capacitances were calculated from the GCD curves, as shown in Fig. S3 (d). The electrochemical properties at different voltage ranges, such as 0–1 V (Fig. S4) and 2–4.25 V (Fig. S5), are shown in the Supporting Information. Notably, the cells operated effectively for both high-and low-voltage ranges.

The CV curves with and without light illumination exhibited similar shapes (Fig. S3(a)). However, the CV characteristics of the cell measured under light illumination showed a larger curve area than those measured without illumination, indicating that optical illumination enhanced the specific capacitance. The GCD curves with and without light illumination had similar triangular shapes. Moreover, the cell exhibited high performance up to a high current density of 32 mA/cm^2 in the 0–4 V voltage range under light ON conditions; however, without light

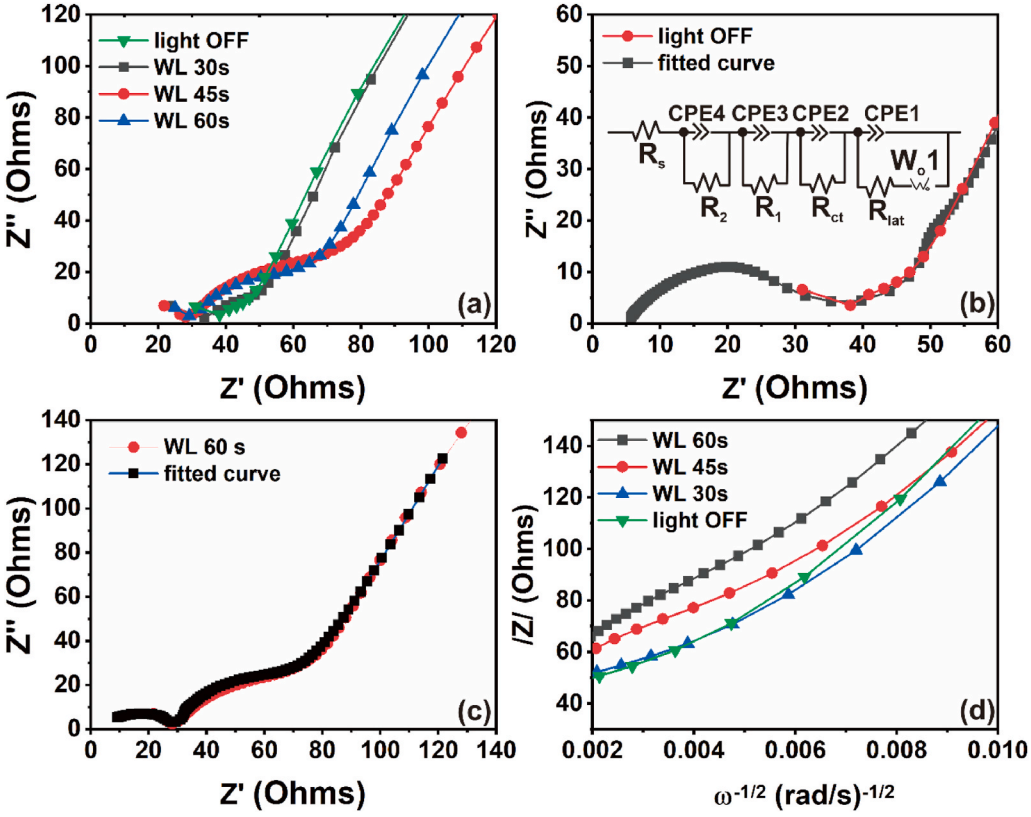

Fig. 3. (a) Nyquist plot of electrochemical impedance spectroscopy (EIS) with and without light illumination, (b–c) impedance spectra and the fitted curves under light illumination, (d) $|Z|$ vs (angular freqeuncy)$^{-1/2}$ curves (frequency region 1–40 kHz) with and without light illumination from which the diffusion coefficient is calculated. The inset of (b) shows the circuit model used to fit the Nyquist plots shown in (b–c). WL 30 s, WL 45 s, and WL 60 s correspond to the impedance spectra recorded after 30, 45, and 60 s of light illumination, respectively.

illumination, the cell could only operate up to a current density of 16 mA/cm^2.

For non-symmetric GCD curves, the capacitance (C) and energy density (E), and Power density (P) is given by [30],

$$C_{areal} = \frac{2i_a \int Vdt}{V^2\big|_{v_i}^{v_f}} \quad C_{vol} = \frac{2i_v \int Vdt}{V^2\big|_{v_i}^{v_f}} \tag{1}$$

$$E_{areal} = i_a \int VdtE_{vol} = i_v \int VdtE_{gra} = i_m \int Vdt \tag{2}$$

$$\text{Power density, } P_{areal} = \frac{E_{areal}}{t} \quad P_{vol} = \frac{E_{vol}}{t} \tag{3}$$

Where C_{areal} (F/cm^2), C_{vol} (F/cm^3) are the areal and volumetric, capacitances, E_{areal} (Wh/cm^2) E_{vol} (Wh/cm^3), are the areal, and volumetric energy densities, and P_{areal} (W/cm^2), P_{vol} (Wh/cm^3), are the areal and volumetric. $i_{areal} = I/A$ (A/cm^2), $i_v = I/V$ (A/cm^3), are the areal and volumetric current densities. $\int$Vdt is the integral area of the discharge curve, V is the potential with v_i and v_f as initial and final values.

For the voltage range of 0–4 V and at a current density of 4 mA/cm^2, the areal energy density values were 148 μWh/cm^2 and 40 μWh/cm^2 with and without light, respectively. With light, the cell functioned up to 32 mA/cm^2 with a maximum areal power density of 64 mW/cm^2.

For the voltage range of 2–4.25 V and at a current density of 4 mA/cm^2, the areal energy density values were found to be 233 μWh/cm^2 and 91 μWh/cm^2 with light and without light, respectively. With light, the cell could operate up to 40 mA/cm^2 with a maximum areal power density of 45 mW/cm^2 Without light, the cell only functioned up to 32 mA/cm^2 with a maximum areal power density of 36 mW/cm.^{2}

The areal/volumetric/gravimetric energy densities, power densities, and capacitances of the cell with and with out light are listed in Tables S1–4. Under light illumination, the cell operated at a high voltage range (0–4 V) and a high current density (40 mA/cm^2). Notably, compared to the cell operated without light, the illuminated cell could operate at higher current densities for all voltage windows used in this study.

Nyquist plots (electrochemical impedance spectroscopy) were recorded and extensively analysed to gain insight into the exceptional performance of the fabricated cells, as shown in Fig. 3. The Nyquist plot provides a better understanding of the electrode-electrolyte interface. Fig. 3(a) shows the Nyquist diagrams of the cell showing the imaginary part (Z'') vs. the real part (Z′) of the impedance with light (WL 30 s, WL 45 s, and WL 60 s) and without light (light OFF) illumination. Fig. 3(b and c) show the fitted Nyquist plots recorded without light and WL 60 s, respectively. All the Nyquist plots were fitted using the equivalent circuit model shown in the inset of Fig. 3(b) consisting of resistances (R_s, R_{ct}, R_{lat}, R_1, and R_2), constant phase elements (CPEs), such as CPE1, CPE2, CPE3, and CPE4, and Warburg impedance (W_O). R_s is the solution resistance, R_{ct} is the charge transfer resistance at the electrode surface/solution interface, R_{lat} is the resistance of the intercalation lattice, and R_1 and R_2 are the additional resistances formed during the light-induced intercalation of electrolyte ions deep into the electrode layers.

The fitted Nyquist plots of WL 30 s and WL 45 s are shown in Fig. S6. In the high-frequency region (1–100 MHz), an intercept on the real axis provides R_s, and the semi-circle feature reflects R_{ct}. The Warburg diffusion in the mid-frequency region (10–200 kHz) is attributed to the ion diffusion of electrolytes in the active materials. The Nyquist plots recorded under light illumination (WL 30 s, WL 45 s, and WL 60 s) confirmed that the R_s and R_{ct} values decreased with prolonged light illumination. The CPEs depicted the non-ideal capacitance behavior of the electrolyte/electrode interface. The fitted curves were well-matched with the corresponding recorded spectra. The fitted equivalent circuit parameters are presented in Table S5, and clearly show an increase in capacitance (CPE3 and CPE4) with prolonged light illumination. However, considerable decreases in R_{lat} (8 Ω (light OFF) to 2.5 Ω (WL 60 s), W_O (7 Ω (light OFF) to 0.6 mΩ (WL 60 s)), and Warburg diffusion time, *Wo-1-T* ((4 × 10^{-7} s (light OFF) to 4.98 × 10^{-12} s (WL 60 s)) were also

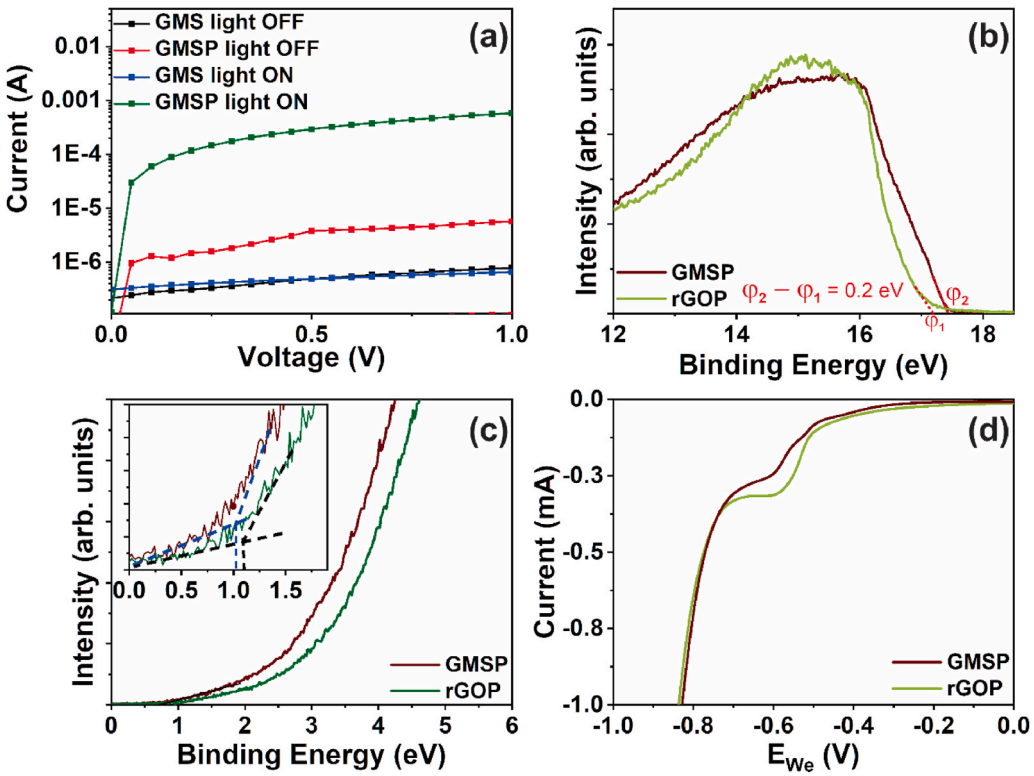

Fig. 4. (a) Current-voltage characteristics of rGO and GMSP samples under light illumination, (b) ultraviolet photoemission spectroscopy (UPS) spectra of GMSP and rGOP samples, (c) kinetic energy cut-off of the secondary electron, and (d) cyclic voltammetry curves (current vs. working electrode potential, E_{we}) at a scan rate of 20 mV/s for reduction processes.

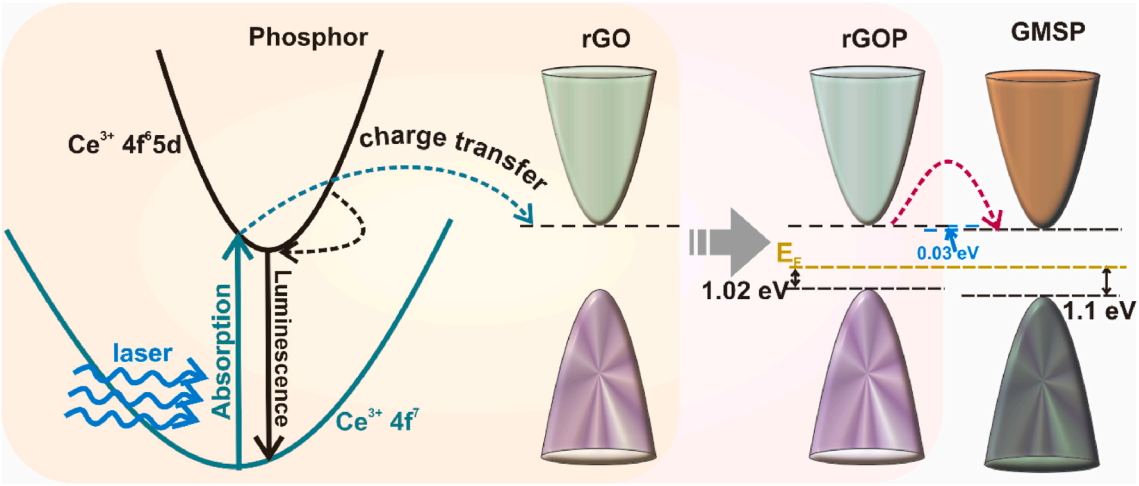

Fig. 5. Schematic diagram of the photoconductivity and charge transfer process in the rGOP layer to GMSP.

observed. Notably, the CPE4 and CPE3 values were very low without light illumination. However, under prolonged light illumination, the CPE4 and CPE3 values increased rapidly. The W_O value in the mid-frequency region could be attributed to the diffusion process, and a significant variation in the diffusion region with illumination can be observed in Fig. 3(a). Thus, the increase in CPE4 and CPE3 indicated that further diffusion of the electrolyte ions occurred under light illumination, resulting in additional capacitance.

The diffusion coefficient of electrolyte ions in the electrode material with and without light illumination can be calculated from the impedance data at lower frequencies using previously suggested methods.

The magnitude of the impedance is given by

$$|Z| = \frac{T}{C_T (D\cdot\omega)^{1/2}} \tag{4}$$

Imaginary part of impedance is given by,

$$\mathrm{Im}\, Z = \frac{1}{C_T \omega} \tag{5}$$

where, T, C_T, and D are the film thickness, low-frequency redox capacitance, and diffusion coefficient, respectively. The plot of $|Z|$ vs. $\frac{1}{\omega^{0.5}}$ with and without light (frequency region 1–40 kHz) is shown in Fig. 4(f), and the slope of the curve provides $\frac{T}{C_T D^{1/2}}$. The plot of Im{Z} vs. $\frac{1}{\omega}$ with and

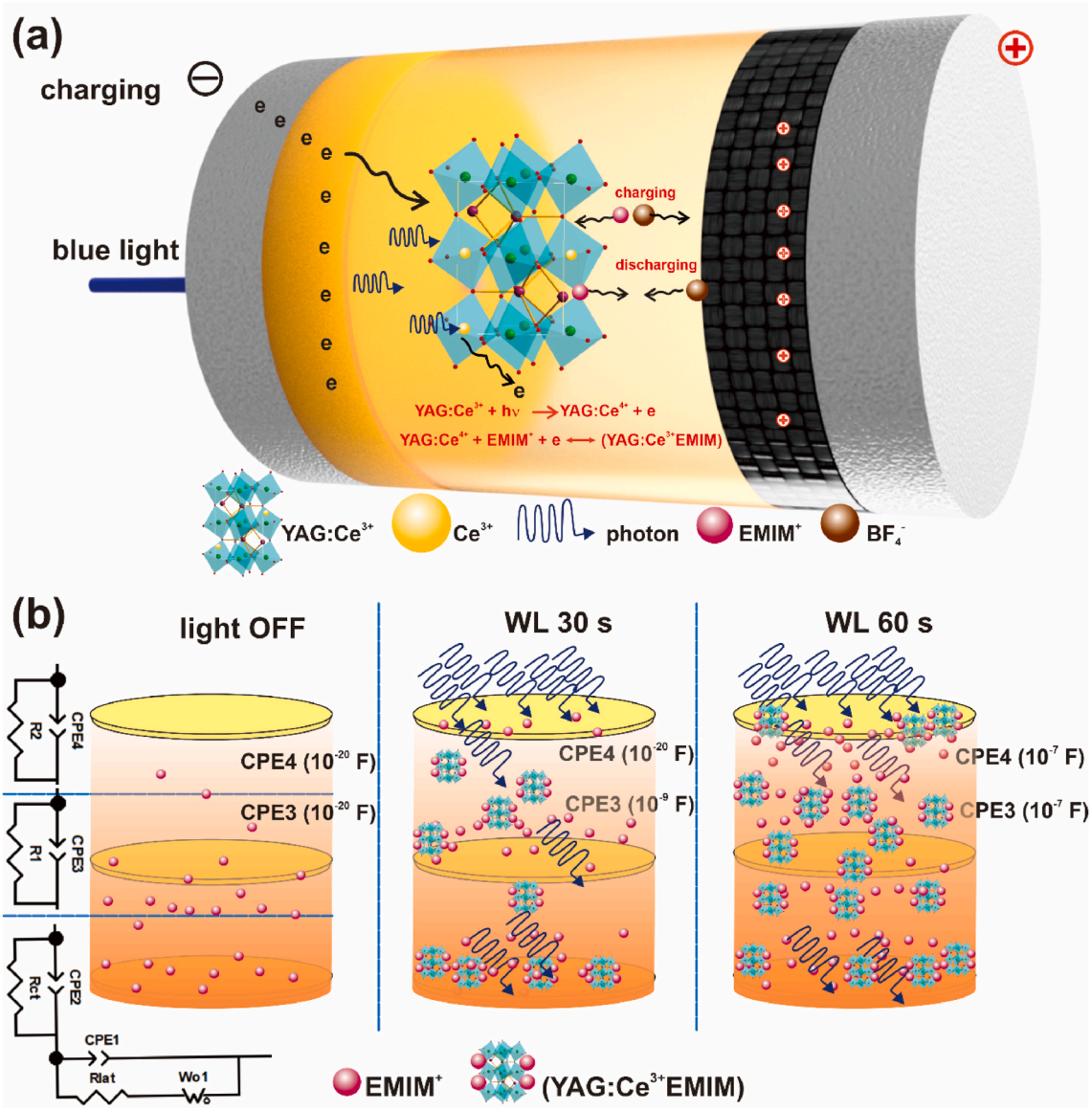

Fig. 6. (a) Schematic diagram of the light-induced voltage developed under light illumination. (pink spheres denote EMIM yellow spheres denote Ce^{3+} and brown spheres denote BF_4^-) (b) Diffusion of electrolyte ions in the electrode material under light OFF and light ON for 30 s and 60 s. (For interpretation of the references to colour in this figure legend, the reader is referred to the Web version of this article.)

without light is shown in Fig. S7, and the slope of the curve provides $\frac{1}{C_T}$. The diffusion coefficients were calculated from both slope values and were found to be 106.33 × 10^{-6}, 133.06 × 10^{-6}, 144.6 × 10^{-6}, and 156.92 × 10^{-6} m^2/s for light OFF, WL 30 s, WL 45 s, and WL 60 s, respectively. This clearly showed that the *D* increased under light illumination. The increase in D might originate from the thermal effect of the laser heating due to prolonged illumination. However, further studies are required to investigate the exact reason for the increase in D value during light illumination.

Impedance spectroscopy analysis revealed that the superior performance of the light-controlled capacitors could be attributed to the (i) decrease in R_s leading to enhanced electrode conductivity, and (ii) significant decrease in W_O, *Wo-1-T*, and R_{lat}, and an increase in *D*.

To identify the factors leading to the enhancement of the electrode conductivity (decrease in R_s), the current-voltage characteristics of the electrode material were measured with and without light illumination (Fig. 4(a)). The conductivity increased sharply (10^2 times) in the GMSP sample under light illumination. The absorbed photons in YAG:Ce^{3+} excite electrons from the ground state to the excited state. In the absence of an external electric field/voltage these electrons de-excite and emits the photons in the visible range, which is utilised in light-emitting diodes. The photoluminescent excitation and emission spectra of the YAG:Ce^{3+} phosphor are shown in Fig. S8. However, under an applied electric field, those photo-excited electrons are swept away by the applied voltage, increasing the net conductivity of the GMSP. The photo-excitation of Ce^{3+} ions in the phosphor generated free electrons, leading to a higher carrier density and higher conductivity in GMSP. The excitation band of Ce^{3+} matched well with the emission wavelength of the blue laser diode (450 nm), resulting in efficient absorption of blue light, and thus, high conductivity. The absorption spectrum of undoped YAG is approximately 190 nm; therefore, 450 nm light illumination using a laser diode does not affect the YAG matrix.

The transport of electrons from the rGOP layer to the GMSP layer requires an appropriate energy-band alignment. To calculate the work function and analyse the energy band alignment, the highest occupied molecular orbit (HOMO) to lowest unoccupied molecular orbit (LUMO) levels in rGOP and GMSP were estimated from the ultraviolet photo-emission spectroscopy (UPS) spectra and three-electrode CV

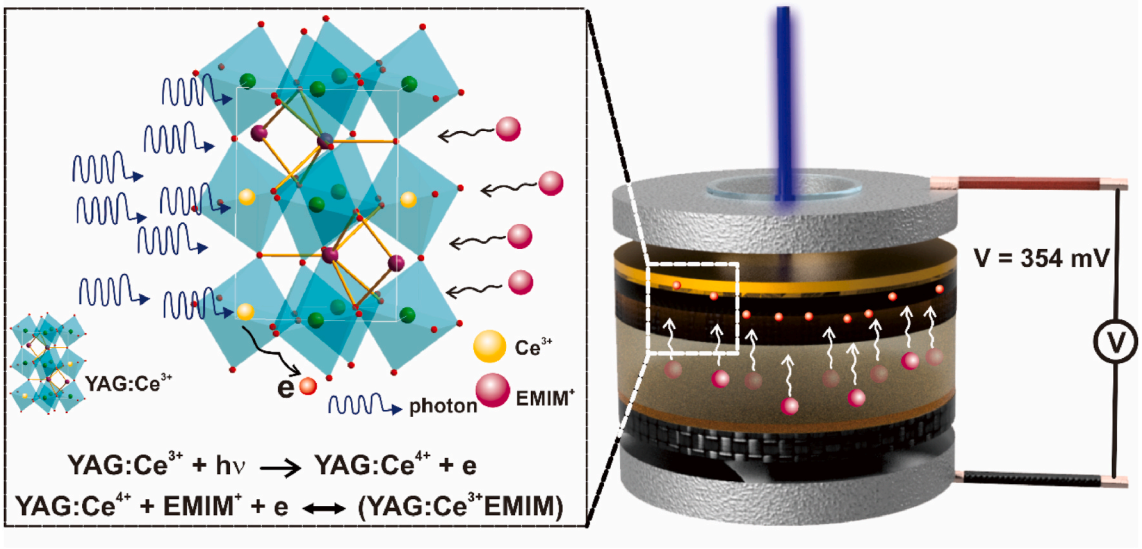

Fig. 7. Schematic of the light-induced charged voltage developed under light illumination. (The pink spheres denote EMIM yellow spheres denote Ce^{3+} and the orange spheres denote electrons). (For interpretation of the references to colour in this figure legend, the reader is referred to the Web version of this article.)

Table 1
A comparison of the performance parameters of the proposed supercapacitor with the recently reported supercapacitors.

Material	Current density (mA/cm^2)	Capacitance (mF/cm^2)	Energy density μWh/cm^2)	Power density (mW/cm^2)	Reference
S-α-Fe_2O_3@C/OCNTF	2	201.3	135.3	2.19	[36]
Zn-ion hybrid MSCs	0.16	1297	115.4	0.16	[37]
siloxene sheets based symmetric supercapacitor	–	2.18	2.72	0.2	[38]
PEDOT NW film-based SC	1	413.5	48.3	0.22	[39]
graphene foam-based supercapacitor	0.67	38	3.4	0.27	[40]
CH NTAs@NiAl LDH NSs based SC	2	586	181.9	1.45	[41]
Flexible textile-based supercapacitors	1	245.5	21.82	0.4	[42]
CH NTAs/CF-based supercapacitor	1	–	93.8	0.193	[43]
($CoMoO_4$@$Co(OH)_2$) core–shell structure based SC	2	536	167.5	1.5	[44]
NC LDH NSs@Ag@CC) based SC	1	230.2	78.8	0.785	[45]
rGO/PPy composite electrodes based SC	0.1	222	20	0.04	[46]
GMSP electrodes based SC	4	331	233	9.7	This study

measurements, which are shown in Fig. 4(b–d). The work function difference (φ_2 - φ_1) between the rGOP and the GMSP was 0.2 eV, which was calculated from the secondary cut-off at a high binding energy [31], as shown in Fig. 4(b) (red dotted lines). Additionally, the HOMO level [31] of rGOP and GMSP are 1.02 eV and 1.1 eV below the Fermi level (E_F), respectively (Fig. 5(c)). The HOMO values were determined from the extrapolated value of the intercept [31–33] (see Fig. 4(c)). The cyclic voltammetry reduction curve can be used to determine the LUMO energy level [34,35].

According to the onset potential of the reduction processes, the difference in the LUMO levels of rGOP and GMSP was 0.03 eV (Fig. 4(d)). This indicated a reasonable energy band alignment between the rGOP layer and GMSP, which facilitated electron transfer between them. Notably, both rGO-phosphor and GMSP had similar band alignments, which are entangled.

Thus, additional electrons generated by photo-excitation from the phosphor layer were transported to the GMSP, which enhanced the conductivity. A schematic diagram of the photoconductivity and charge transfer process in the rGOP layer to GMS is shown in Fig. 5.

The significant decrease in the W_O, *Wo-1-T*, and R_{lat}, and an increase in the D reflected the very high rates of Faradaic intercalation redox reactions at the electrode. The enhancement in the Faradaic reaction was attributed to the light-induced oxidation of Ce^{3+} to Ce^{4+} in the phosphor material, resulting in the intercalation of the electrolyte ions ($EMMIM^+$). First, the photo-excitation of Ce^{3+} occurred in the phosphor material ($YAG{:}Ce^{3+} + h\nu \rightarrow YAG{:}Ce^{4+} + e^-$) followed by the redox reaction, as shown in the following chemical equation:

$$YAG{:}Ce^{4+} + EMIM^+ + e \rightleftarrows (YAG{:}Ce^{3+}EMIM) \quad (6)$$

Ce exists as Ce^{3+} in YAG:Ce; therefore, photo-excitation of Ce is a prerequisite for this redox reaction (Ce should exist as Ce^{4+}) because the $Ce^{3+} \rightleftarrows Ce^{2+}$ redox reaction cannot occur. Thus, the extremely high rate of redox reactions occurring between Ce^{4+} ions in YAG and $EMIM^+$ resulted in the significant changes in W_O, *Wo-1-T*, R_{lat}, and D

Fig. 6(a) shows a schematic of the Faradaic redox reaction in the electrode material under light illumination.

The prolonged diffusion of the electrolyte ions toward the phosphor layer under continuous light illumination is schematically shown in Fig. 6(b). Under prolonged light illumination, owing to the light-induced redox reaction, the electrolyte ions diffuse deeper into the phosphor layer, resulting in enhanced capacitance, energy, and power density values.

The capacitance and energy density could have increased owing to two reasons: (i) enhanced conductivity and (ii) enhanced redox reaction. Thus, visible light was successfully utilised to enhance the energy density of a supercapacitor by three-fold compared to that achieved under dark conditions.

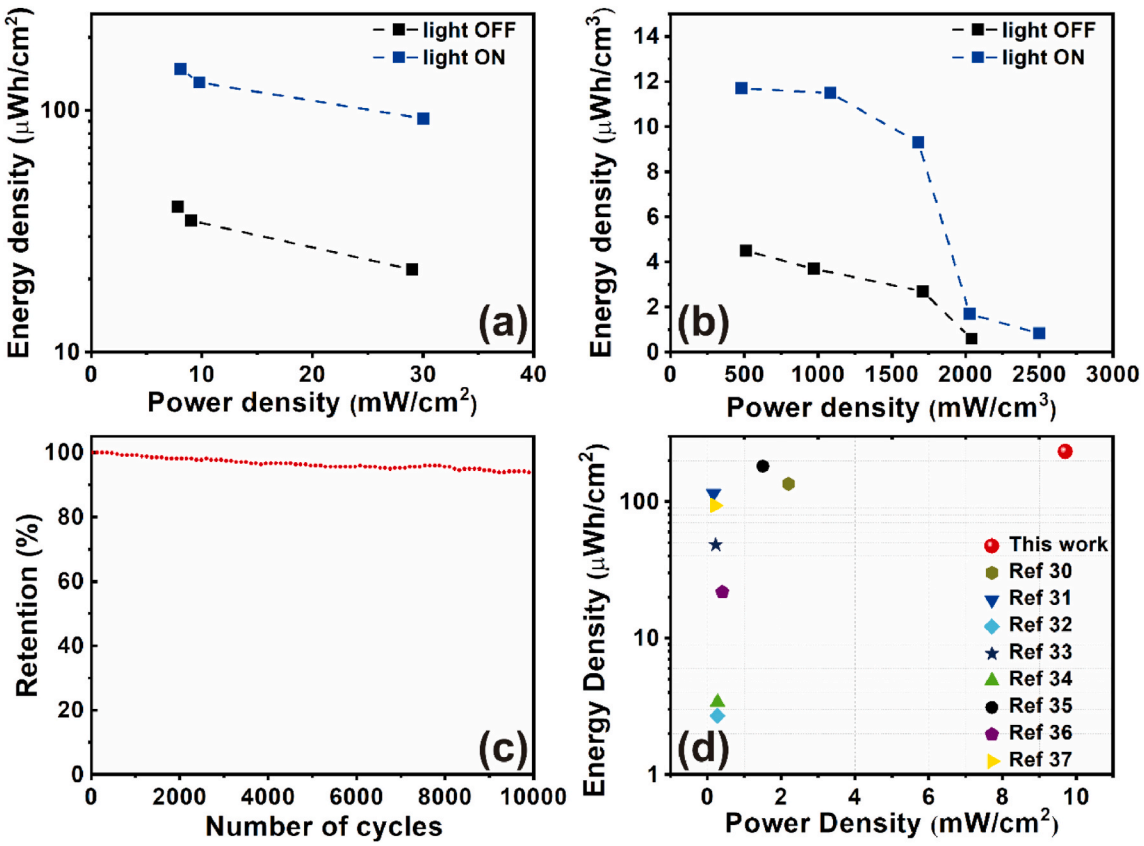

Fig. 8. (a) Areal Ragone plots with and without light for the cell in voltage window regions 0–4 V, (b) volumetric Ragone plots with and without light in voltage window regions 2–4.25 V, (c) electrochemical stability of the cell with light, (d) Ragone plot indicating energy density vs. power density of the fabricated cell (2–4.25 V window) compared with values reported in other literature [36–43].

3.1. Light-induced charging properties of the cell

Because an enhancement was achieved in the energy density and capacitance values under light illumination, the light-induced-charging characteristics of the cell were investigated by illuminating the device with blue laser light (without any external bias). The open-circuit voltage during light-induced charging with light is shown in Fig. S9. The GCD properties measured during light-induced charging are shown in Fig. S10. After light-induced charging without any external bias, the cell was discharged to its initial state using a discharge current of 100 nA, We charged up to 354 mV with light ON for 15 min. Notably, under light illumination, the voltage of the cell continuously increased without any external charging source. It is clear from the previous discussions that light-induced charging occurred due to a light-induced Faradaic intercalation redox reaction. Light illumination triggers the $Ce^{3+} \rightarrow Ce^{4+}$ oxidation, followed by the release of an electron resulting in the Faradaic redox reaction with the $EMIM^{+}$ ions. Fig. 7 shows a schematic of the light-induced charging process.

The light-induced charging voltage of the fabricated cell is comparable with that of recently reported studies where light-induced charging was achieved via other methods, using piezoelectric-driven (112 mV, 110 mV, and 207 mV) [24,26,27] and conducting polymers (48 mV) [25]. Fig. S11 shows a digital photograph representing the measurement of the light-induced charged voltage with light, without any external bias. Thus, light-induced charging was achieved in the proposed supercapacitor by simply including an additional phosphor layer.

A comparison of the performance parameters of the recently reported supercapacitors is shown in Table 1. It is worth noting that, at a current density of 4 mA/cm^2, the energy and power density of the supercapacitor were significantly higher than the previously reported values, and the fabricated cell could operate up to a higher current density of 40 mA/cm^2.

Areal Ragone plots with and without light for the cell in voltage window regions 0–4 V and volumetric Ragone plots with and without light in voltage window regions 2–4.25 V are shown in Fig. 8(a and b), respectively. The cell exhibited excellent and stable cycling performance (Fig. 8(c)) under optical illumination. The cycling performance of the cell indicated that the cell maintained 93% of its initial capacitance after 10,000 cycles. The coulombic efficiency is shown in supporting Fig. S12. The Ragone plot shown in Fig. 8(d) compares the energy density vs. power density of the fabricated cell with those of previously reported supercapacitors, demonstrating the superior performance of cells fabricated in this study that can harvest visible light.

A three-fold enhancement in the energy density was achieved under light illumination in the 0–4 V, 2–4.25 V, and 0–1 V voltage window regions. The enhancement in the energy/power density indicated that visible light illumination could effectively increase the charge storage capacity/energy density of the supercapacitors reported herein. Hence, through proper optimisations, visible light could be used to charge portable devices and provide a method for the development of next-generation self-powered supercapacitor devices.

4. Conclusions

The present study successfully harvested visible light to improve the energy density and light-induced charging capacity of a supercapacitor by including a phosphor layer over the electrodes. A rGO-coated phosphor layer was deposited on top of the GMSP electrodes. For facilitating light illumination, a stainless-steel case equipped with a quartz window was used. When illuminated with a blue laser diode, the supercapacitor exhibited an energy density of 233 $\mu Wh/cm^2$ at a current density of 4

mA/cm^2. The fabricated cell could operate over a high voltage range (0–4 V) and high current density (40 mA/cm^2). The operating current densities of the cell under light illumination were approximately twice as those without light illumination. The achieved energy density under light illumination was approximately 2.5 times higher than that achieved without light illumination. The high energy density was achieved owing to the generation of photocarriers and a light-induced Faradaic intercalation redox reaction at the electrode-electrolyte interface. The generated photocarriers were successfully utilised to enhance the storage capacity of the supercapacitor through Faradaic diffusion. EIS analysis confirmed that the diffusion of electrolyte ions was enhanced by light illumination. The light-induced Faradaic redox reaction and diffusion also led to charging of the supercapacitors. Moreover, solar energy could be utilised instead of blue laser light to achieve a higher energy density in supercapacitors, and the transparent nature of the quartz window could be utilised to develop portable self-charging devices with high energy density.

CRediT authorship contribution statement

Janardhanan R. Rani: Visualization, Investigation, Conceptualization, Methodology, Formal analysis, Writing – original draft, Writing – review & editing. **Nayan Chandra Das:** Methodology. **Minjae Kim:** Resources, Data curation. **Ranjith Thangavel:** Methodology, Resources, Data curation. **Sung Tae Kim:** Resources, Supervision. **Yun Sung Lee:** Writing – review & editing. **Jae-Hyung Jang:** Supervision, Funding acquisition, Writing – review & editing.

Declaration of competing interest

The authors declare the following financial interests/personal relationships which may be considered as potential competing interests: Jae-Hyung Jang reports financial support was provided by National Research Foundation of Korea.

Data availability

Data will be made available on request.

Acknowledgments

This work was supported by the Creative Materials Discovery Program (2017M3D1A104088) through the National Research Foundation of Korea (NRF) and 'Regional Innovation Mega Project' (2023-DD-UP-0015) through the Korea Innovation Foundation funded by Ministry of Science and ICT and Jeollanam-do.

Appendix A. Supplementary data

Supplementary data to this article can be found online at https://doi.org/10.1016/j.jpowsour.2023.233197.

References

[1] C. Allen, G. Metternicht, T. Wiedmann, Environ. Sci. Pol. 66 (2016) 199–207.
[2] M. Sevilla, R. Mokaya, Energy Environ. Sci. 7 (2014) 1250–1280.
[3] A. Ghorai, A. Midya, S.K. Ray, New J. Chem. 42 (2018) 3609–3613.
[4] M. Duraivel, S. Nagappan, B. Balamuralitharan, S. Selvam, S.N. Karthick, K. Prabakar, C.-S. Ha, H.-J. Kim, New J. Chem. 42 (2018) 11093–11101.
[5] L.-W. Chong, H.-T. Chien, Y.-L. Lee, J. Power Sources 195 (2010) 5109–5113.
[6] C. Ogata, R. Kurogi, K. Hatakeyama, T. Taniguchi, M. Koinuma, Y. Matsumoto, Chem. Commun. 52 (2016) 3919–3922.
[7] G. Wang, L. Zhang, J. Zhang, Chem. Soc. Rev. 41 (2012) 797–828.
[8] P. Asen, S. Shahrokhian, A.I. zad, J. Electroanal. Chem. 823 (2018) 505–516.
[9] W. Shi, B. Chang, H. Yin, S. Zhang, B. Yang, X. Dong, Sustain. Energy Fuels 3 (2019) 1201–1214.
[10] X. Cheng, X. Gui, Z. Lin, Y. Zheng, M. Liu, R. Zhan, Y. Zhu, Z. Tang, J. Mater. Chem. 3 (2015) 20927–20934.
[11] S.M. Pourmortazavi, M. Rahimi-Nasrabadi, M.S. Karimi, S. Mirsadeghi, New J. Chem. 42 (2018) 19934–19944.
[12] B. Bhujun, M.T.T. Tan, A.S. Shanmugam, Results Phys. 7 (2017) 345–353.
[13] P. Ahuja, R.K. Sharma, G. Singh, J. Mater. Chem. 3 (2015) 4931–4937.
[14] F. Markoulidis, C. Lei, C. Lekakou, D. Duff, S. Khalil, B. Martorana, I. Cannavaro, Carbon 68 (2014) 58–66.
[15] H. Cao, X. Peng, M. Zhao, P. Liu, B. Xu, J. Guo, RSC Adv. 8 (2018) 2858–2865.
[16] A. Gopalakrishnan, C.Y. Kong, S. Badhulika, New J. Chem. 43 (2019) 1186–1194.
[17] Y. Luo, Q.e. Zhang, W. Hong, Z. Xiao, H. Bai, Phys. Chem. Chem. Phys. 20 (2018) 131–136.
[18] L. Wang, C. Zhang, X. Jiao, Z.J.N.R. Yuan, 12 (2019) 1129-1137.
[19] F. Mokhtari, Z. Cheng, R. Raad, J. Xi, J. Foroughi, J. Mater. Chem. 8 (2020) 9496–9522.
[20] R. Song, H. Jin, X. Li, L. Fei, Y. Zhao, H. Huang, H. Lai-Wa Chan, Y. Wang, Y. Chai, J. Mater. Chem. 3 (2015) 14963–14970.
[21] G. Anoop, J.R. Rani, J. Lim, M.S. Jang, D.W. Suh, S. Kang, S.C. Jun, J.S. Yoo, Sci. Rep. 6 (2016), 33993.
[22] G. Anoop, I.H. Cho, D.W. Suh, J.S. Yoo 209 (2012) 2635–2640.
[23] D.C. Marcano, D.V. Kosynkin, J.M. Berlin, A. Sinitskii, Z. Sun, A. Slesarev, L. B. Alemany, W. Lu, J.M. Tour, ACS Nano 4 (2010) 4806–4814.
[24] K. Krishnamoorthy, P. Pazhamalai, V.K. Mariappan, S.S. Nardekar, S. Sahoo, S.-J. Kim, Nat. Commun. 11 (2020) 2351.
[25] Y. Yin, K. Feng, C. Liu, S. Fan, J. Phys. Chem. C 119 (2015) 8488–8491.
[26] S. Sahoo, K. Krishnamoorthy, P. Pazhamalai, V.K. Mariappan, S. Manoharan, S.-J. Kim, J. Mater. Chem. 7 (2019) 21693–21703.
[27] A. Ramadoss, B. Saravanakumar, S.W. Lee, Y.-S. Kim, S.J. Kim, Z.L. Wang, ACS Nano 9 (2015) 4337–4345.
[28] J.R. Rani, R. Thangavel, M. Kim, Y.S. Lee, J.-H. Jang, Nanomaterials 10 (2020) 2049.
[29] J.R. Rani, S.-I. Oh, J.M. Woo, N.L. Tarwal, H.-W. Kim, B.S. Mun, S. Lee, K.-J. Kim, J.-H. Jang, ACS Appl. Mater. Interfaces 7 (2015) 5693–5700.
[30] L.-Q. Mai, A. Minhas-Khan, X. Tian, K.M. Hercule, Y.-L. Zhao, X. Lin, X. Xu, Nat. Commun. 4 (2013) 2923.
[31] C. Wang, D. Niu, B. Liu, S. Wang, X. Wei, Y. Liu, H. Xie, Y. Gao, J. Phys. Chem. C 121 (2017) 18084–18094.
[32] J.M. Lee, J.H. Baek, T.M. Gill, X. Shi, S. Lee, I.S. Cho, H.S. Jung, X. Zheng, J. Mater. Chem. 7 (2019) 9019–9024.
[33] M.J. Al-Saadi, S.H. Al-Harthi, H.H. Kyaw, M.T.Z. Myint, T. Bora, K. Laxman, A. Al-Hinai, J. Dutta, Nanoscale Res. Lett. 12 (2017) 22.
[34] P. Gasiorski, K.S. Danel, M. Matusiewicz, T. Uchacz, W. Kuźnik, A.V.J.J.o.F. Kityk, 22 (2012) 81-91.
[35] A. Bayat, E. Saievar-Iranizad, J. Lumin. 192 (2017) 180–183.
[36] Z. Zhou, Q. Zhang, J. Sun, B. He, J. Guo, Q. Li, C. Li, L. Xie, Y. Yao, ACS Nano 12 (2018) 9333–9341.
[37] P. Zhang, Y. Li, G. Wang, F. Wang, S. Yang, F. Zhu, X. Zhuang, O.G. Schmidt, X. Feng, Adv. Mater. 31 (2019), 1806005.
[38] K. Krishnamoorthy, P. Pazhamalai, S.-J. Kim, Energy Environ. Sci. 11 (2018) 1595–1602.
[39] D. Ni, Y. Chen, H. Song, C. Liu, X. Yang, K. Cai, J. Mater. Chem. 7 (2019) 1323–1333.
[40] L. Manjakkal, C.G. Núñez, W. Dang, R. Dahiya, Nano Energy 51 (2018) 604–612.
[41] S. Chandra Sekhar, G. Nagaraju, B. Ramulu, S.K. Hussain, D. Narsimulu, J.S. Yu, Nano Res. 12 (2019) 2597–2608.
[42] Z. Li, Y. Ma, L. Wang, X. Du, S. Zhu, X. Zhang, L. Qu, M. Tian, ACS Appl. Mater. Interfaces 11 (2019) 46278–46285.
[43] J.-H. Jeong, J.W. Park, D.W. Lee, R.H. Baughman, S.J. Kim, Sci. Rep. 9 (2019), 11271.
[44] G.K. Veerasubramani, A. Chandrasekhar, S.M. S P, Y.S. Mok, S.J. Kim, J. Mater. Chem. 5 (2017) 11100–11113.
[45] S.C. Sekhar, G. Nagaraju, J.S. Yu, Nano Energy 36 (2017) 58–67.
[46] J. Chen, Y. Wang, J. Cao, Y. Liu, Y. Zhou, J.-H. Ouyang, D. Jia, ACS Appl. Mater. Interfaces 9 (2017) 19831–19842.